Biochimica et Biophysica Acta 1818 (2012) 3131–3140

Contents lists available at SciVerse ScienceDirect

Biochimica et Biophysica Acta

journal homepage: www.elsevier.com/locate/bbamem

Ensemble and single particle fluorimetric techniques in concerted action to study the diffusion and aggregation of the glycine receptor α3 isoforms in the cell plasma membrane

Kristof Notelaers [a,b,1], Nick Smisdom [a,1], Susana Rocha [b], Daniel Janssen [a], Jochen C. Meier [c], Jean-Michel Rigo [a], Johan Hofkens [b], Marcel Ameloot [a,*]

[a] Biomedical Research Institute, Hasselt University and School of Life Sciences, Transnational University Limburg, Agoralaan gebouw C, 3590 Diepenbeek, Belgium
[b] Laboratory for Photochemistry and Spectroscopy, Department of Chemistry, Katholieke Universiteit Leuven, Celestijnenlaan 200F, B-3001 Heverlee, Belgium
[c] RNA Editing and Hyperexcitability Disorders Group, Max Delbrück Center for Molecular Medicine, Robert-Rössle-Strasse 10, 13092 Berlin, Germany

ARTICLE INFO

Article history:
Received 29 March 2012
Received in revised form 3 August 2012
Accepted 11 August 2012
Available online 18 August 2012

Keywords:
Glycine receptor
Alpha3 isoforms
Nanoscopy
Single particle
Ensemble average
Anomalous diffusion

ABSTRACT

The spatio-temporal membrane behavior of glycine receptors (GlyRs) is known to be of influence on receptor homeostasis and functionality. In this work, an elaborate fluorimetric strategy was applied to study the GlyR α3K and L isoforms. Previously established differential clustering, desensitization and synaptic localization of these isoforms imply that membrane behavior is crucial in determining GlyR α3 physiology. Therefore diffusion and aggregation of homomeric α3 isoform-containing GlyRs were studied in HEK 293 cells. A unique combination of multiple diffraction-limited ensemble average methods and subdiffraction single particle techniques was used in order to achieve an integrated view of receptor properties. Static measurements of aggregation were performed with image correlation spectroscopy (ICS) and, single particle based, direct stochastic optical reconstruction microscopy (dSTORM). Receptor diffusion was measured by means of raster image correlation spectroscopy (RICS), temporal image correlation spectroscopy (TICS), fluorescence recovery after photobleaching (FRAP) and single particle tracking (SPT). The results show a significant difference in diffusion coefficient and cluster size between the isoforms. This reveals a positive correlation between desensitization and diffusion and disproves the notion that receptor aggregation is a universal mechanism for accelerated desensitization. The difference in diffusion coefficient between the clustering GlyR α3L and the non-clustering GlyR α3K cannot be explained by normal diffusion. SPT measurements indicate that the α3L receptors undergo transient trapping and directed motion, while the GlyR α3K displays mild hindered diffusion. These findings are suggestive of differential molecular interaction of the isoforms after incorporation in the membrane.

1. Introduction

The diffusion and aggregation of receptors in the cell membrane have received considerable attention in the last decade [1–4]. In addition to endo- and exocytotic cycling of these membrane proteins, their movement and distribution in the plasma membrane can considerably contribute to the homeostasis of these receptors in the membrane [5–7]. In this way, the cell possesses extra tools to fine-tune receptor-mediated signaling events [8–10]. An example of this, is surface trapping of neurotransmitter receptors at post-synaptic sites for the facilitation of neurotransmission [11–14]. Hence, a study of the spatiotemporal membrane behavior of neurotransmitter receptors is important in fully comprehending the physiological receptor function.

The transmembranous glycine receptor (GlyR) α3 is a neurotransmitter receptor subtype for which membrane properties are implicated in regulating signaling events. Post-transcriptional processing of the *GLRA3* gene transcript [15] gives rise to two isoforms identified as GlyRs α3K and α3L [16]. The former is the short isoform exhibiting a diffuse membrane staining and fast desensitization kinetics, while the latter contains a 15 amino acid insert (Fig. 1a), exhibits a clustered membrane appearance and slow desensitization kinetics [16,17]. An altered expression ratio of these isoforms has

Abbreviations: $\langle r^2 \rangle$, mean square displacement; ω_0, laser beam radius at $1/e^2$ of its maximum intensity; CLSM, confocal laser scanning microscope; D′, time-dependent diffusion coefficient; D_{1-3}, diffusion coefficient derived from the time lags 1 to 3; DC, dichroic mirror; dSTORM, direct stochastic optical reconstruction microscopy; FRAP, fluorescence recovery after photobleaching; GlyR, glycine receptor; HA, hemagglutinin; HEK 293, human embryonic kidney 293; ICS, image correlation spectroscopy; MWPR, medium without phenol red; PFA, paraformaldehyde; RICS, raster image correlation spectroscopy; ROI, region of interest; SPT, single particle tracking; TICS, temporal image correlation spectroscopy; TIRFM, total internal reflection fluorescence microscope; t_{lag}, time lag

* Corresponding author at: Agoralaan gebouw C, 3590 Diepenbeek, Belgium. Tel.: +32 11 26 92 33; fax: +32 11 26 92 99.
E-mail address: marcel.ameloot@uhasselt.be (M. Ameloot).

[1] Authors contributed equally.

0005-2736/$ – see front matter © 2012 Elsevier B.V. All rights reserved.
http://dx.doi.org/10.1016/j.bbamem.2012.08.010

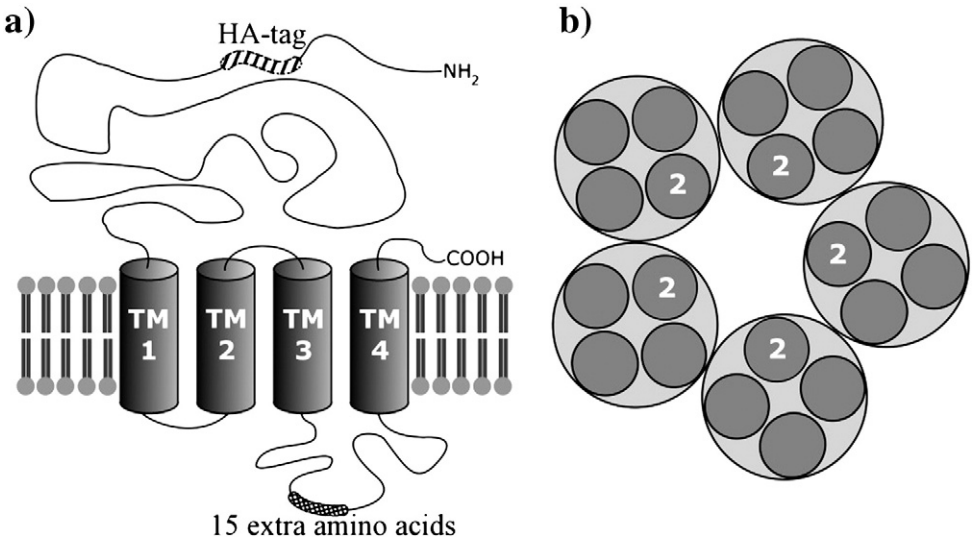

Fig. 1. Schematic representation of the glycine receptor structure. a) General structure of a GlyR subunit showing the four transmembrane α helices (TM1–TM4) and the large, extracellular N-terminal domain. The location of the HA-tag used in this study is indicated, as well as the region of the 15 extra amino acids of the L isoform. b) A functional, homomeric GlyR comprises five subunits, with TM2 of each subunit lining the pore.

been measured in patients with a severe form of temporal lobe epilepsy (TLE) [17–19]. A differential synaptic localization of the isoform subunits, has been associated with this observation [17]. In order to improve the understanding of these isoform-related characteristics, this work investigates the spatiotemporal membrane behavior of homomeric [20] (Fig. 1b) α3K or α3L GlyRs on different time and spatial scales.

The GlyR α3 diffusion and aggregation were studied by means of both ensemble average and single particle fluorimetric techniques, either static or dynamic. Earlier work combining fluorescence recovery after photobleaching (FRAP) [21,22] and single particle tracking (SPT) [23–27] measurements for characterization of protein diffusion was inspirational for our fluorimetric approach [28–30]. In this way an integrated view of receptor properties is obtained and possible technical bias in the interpretation is reduced. However both the confocal laser scanning microscope (CLSM) [31,32] and total internal reflection fluorescence microscope (TIRFM) [33–35], used respectively for FRAP and SPT, provide several more techniques for receptor characterization, without requiring drastic changes to the set-up. In this work the CLSM was used not only for FRAP, but also for image correlation spectroscopy (ICS) [36,37] and raster image correlation spectroscopy (RICS) [38,39]. The range of techniques applied on the TIRFM was extended beyond SPT, with temporal image correlation spectroscopy (TICS) [40,41] and single particle based localization microscopy [42–46], in this case direct stochastic optical reconstruction microscopy (dSTORM) [47–49].

The aggregation state of both α3 isoforms was investigated by ICS and dSTORM. ICS has the advantage that it can be applied on a commercial CLSM and that it can determine the aggregation state of membrane proteins with very low detection limits. However, ICS is diffraction-limited and does not allow for the direct estimation of the cluster size. This hurdle was overcome by dSTORM, which generates a subdiffraction image. Since the biological samples of both techniques are identical, except for the addition of a reducing agent to the measuring solution, the extra workload to apply both techniques is minimal once they are operational. The diffusion of the receptors was studied at various length and time scales using, in order of decreasing scale, FRAP (>1 μm, seconds to minutes), TICS (diffraction limited, ms to s), RICS (diffraction limited, μs to s) and SPT (subdiffraction technique, ms to s). In addition to the different scales they cover, two fundamentally different types of results are obtained: FRAP, TICS and RICS return all an ensemble averaged result, while SPT generates individual information for every tracked particle. For all fluorescence based techniques employed, an organic fluorophore coupled to a primary antibody was used for receptor labeling, allowing for the use of similarly sized labels for all techniques. Furthermore all dynamic measurements were carried out at 37 °C, in order to mimic the effect of body temperature on receptor movement and membrane viscosity.

2. Materials and methods

2.1. Cell culture

Human embryonic kidney 293 cells (HEK 293, kindly provided by Dr. R. Koninckx, Jessa Hospital, Hasselt, Belgium) were maintained at 37 °C in a humidified incubator at 5% CO_2 in Dulbecco's modified eagle's medium (Ref. 41966, Gibco BRL, Paisley, UK) supplemented with 10% fetal calf serum (Biochrom AG, Berlin, Germany) and a penicillin (100 IU/ml)-streptomycin (100 μg/ml) mixture (Invitrogen, Merelbeke, Belgium). The cells used for microscopic observation were plated 2 days before the experiment in 8-well Lab-Tek™ II chambered coverglass (Nalge Nunc International, Rochester, NY, USA) seeded at a density of 20,000 cells per well in transfection medium. This is Dulbecco's modified eagle's medium (Ref. 41965, Gibco BRL, Paisley, UK) supplemented with 10% fetal calf serum but without the penicillin/streptomycin mixture.

2.2. Transfection

After overnight incubation, the cells were transfected using calcium phosphate co-precipitation with plasmids encoding for the hemagglutinin (HA)-tagged (Fig. 1a) splice variants α3K and α3L of the mouse GlyR α3 [17]. The HA-tag was located in the extracellular N-terminal domain between amino acids 35 and 36 [17]. The plasmids were diluted in 250 mM $CaCl_2$ buffer at a concentration of 20 ng/μl and an equal amount of HEPES buffered saline solution (HBS, pH 7.05) was added dropwise. After incubation of 15 min, this mixture was added to the culture medium of the cells. All cell recipients used in the various experiments received a final amount of DNA of 0.21 μg/cm^2. After 6 h, the transfection medium was replaced with transfection medium supplemented with 200 nM strychnine. All measurements occurred within 24 to 36 h after transfection.

2.3. Labeling of exogenous GlyRs

A chicken polyclonal anti-HA antibody (Bethyl lab Inc., Montgomery, TX, USA) was used to stain the HA-tagged GlyRs. This antibody was directly labeled with Alexa Fluor 488 (Alexa 488) or Alexa Fluor 647 (Alexa 647) using a commercial Alexa Fluor 488/647 tetrafluorophenyl labeling kit (Molecular Probes/Invitrogen) according to the manufacturer's protocol. Two vials of reactive fluorochrome were used to increase the degree of labeling. The degree of labeling was determined using a Nanodrop ND-1000 spectrophotometer (Thermo Scientific, Wilmington, DE, USA) at 3.9 (Alexa 488) and 4.4 (Alexa 647) labels per antibody. Cells transfected with the GlyR α3 were rinsed twice with HEPES-buffered DMEM without phenol red (Ref. 21063, Gibco), abbreviated as MWPR (medium without phenol red), and incubated for 10 min at 37 °C with a 4 μg/ml (Alexa 488) and 2 μg/ml (Alexa 647) antibody solution. Afterwards, cells were rinsed three times with MWPR and used for live cell imaging (FRAP, RICS, TICS, SPT) or fixed for 10 min using 4% (w/v) paraformaldehyde (PFA) in phosphate buffered saline (ICS, dSTORM).

2.4. Image correlation spectroscopy

Bottom membrane images of fixed cells were acquired using a Zeiss LSM 510 META (Carl Zeiss, Jena, Germany) CLSM on an inverted epifluorescence Axiovert 200M motorized frame equipped with an αPLAN-APOCHROMAT 100×/1.46 objective (Carl Zeiss). 150 fs pulsed laser light of a Titanium:Sapphire laser (Mai Tai, Spectra-Physics, Irvine, CA, USA) tuned at an output wavelength of 930 nm (1.4 W output power) with 1.5 mW on the stage was used to excite Alexa 488. The emission light was detected using non-descanned detection: the fluorescence was directed using a dichroic mirror (DC) FT685, a short-pass KP685 and a band-pass BP495-545 towards a photomultiplier tube (PMT; Hamamatsu 7422, Herrsching am Ammersee, Germany). This PMT was connected to an SPC830 card (Becker and Hickl, Berlin, Germany) synchronized by the scan pulses from the CLSM. Data were acquired in FIFO imaging mode. The resulting images have a 512 by 512 resolution, a pixel size of 22 nm, and a pixel dwell time of 51.2 μs. Data were analyzed using in-house developed routines written in a MATLAB® environment (R2010b, The Mathworks, Gouda, The Netherlands) according to a published protocol for ultrasensitive detection [37].

2.5. Direct stochastic optical reconstruction microscopy

Transfected cells were stained with Alexa 488 and fixed prior to incubation with a buffered solution containing 100 mM cysteamine (Sigma-Aldrich). dSTORM was carried out on these cells at room temperature using an inverted epi-fluorescence microscope (Olympus IX71 frame S1F-3, Olympus Optical, Tokyo, Japan) equipped with a PlanApo 60× oil objective (NA 1.45; Olympus Optical). The beams of a 100 mW 488 nm (Excelsior 488, Spectra-Physics) and a 100 mW 405 nm (Cube Coherent) diode laser were consecutively selected by mechanical shutters during respectively 50 and 40 ms at a repetition rate of 10 Hz. This light was directed by the DC (z405/491rdc; Chroma, Bellow Falls, VT, USA) towards the objective in off-axis mode to obtain total internal reflection. Excitation light was removed using the DC and a HQ500LP emission filter (Chroma). The 488 nm excitation light was used to excite the Alexa 488 and to obtain a suitable off switching rate. The on switching rate was controlled by the 405 nm laser light with 40 ms exposure time in the overall sequence [50]. The images were recorded at 10 Hz using an EM-CCD camera (ImageEM, Hamamatsu) with 50 ms integration time, a resolution of 512×512 and an image pixel size of 80 nm. The camera was synchronized with the exposure time of the 488 nm laser light, reducing additional background introduced by the 405 nm light exposure. Using home-developed software the particle positions were determined and mapped out on a 20 nm pixel grid corresponding to the localization precision [51,52]. Multi-distance spatial clustering analysis was performed on the obtained point maps using Ripley's H-function [53]. This function is derived from Ripley's K-function [54,55], but represents clustering and dispersions by means of positive and negative values respectively.

2.6. Fluorescence recovery after photobleaching

FRAP measurements were performed using a Zeiss LSM 510 META CLSM (Carl Zeiss) on an epifluorescence Axiovert 200 M motorized frame. The Alexa 488 was excited with the 488 nm line (selected by a 488 ± 10 nm interference-base laser cleanup filter) of the 30 mW air-cooled argon ion laser (5.5 A tube-current) under the control of an AOTF (set at 0.8% transmission). The excitation light was directed to the sample via a DC (HFT 488) and a Plan-Neofluar 40×/1.3 oil immersion objective (Carl Zeiss). The fluorescence light was detected in descanned mode through the DC and a long-pass LP505 emission filter to the PMT. The pinhole size was set to 3 Airy units and the image size was typically set to 512×512 pixels with a pixel size of 63 nm. The interval between the start of subsequent frames was determined as 1/3 τ_D. Each time series typically comprised 2 pre-bleach frames and 18 recovery frames. Cells were kept at 37 °C by means of a small stage incubator and an objective heater (Pecon, Erbach, Germany). Resulting time series were analyzed using custom written routines in a MATLAB environment based on published software components [22]. A new approach was introduced to select a reference region that comprises the bleach region of interest (ROI) and its perimeter in which the fluorescence can be assumed to be constant after bleaching occurred. This approach allows extraction of the recovery curve without user biased selection of a reference region and finds its origin in a procedure suggested by Phair [56,57] (Supplementary material 1). Two FRAP models are used in the analysis step: the uniform disk model [58] and the generalized disk model [22]. The latter model was implemented with the instrumental resolution factor fixed at the estimated value of 0.07 μm^2.

2.7. Raster image correlation spectroscopy

The RICS measurements were performed with the identical setup as used for ICS. A small stage incubator and an objective heater (Pecon) were used to keep the cells at 37 °C. Besides the αPlan-Apochromat 100×/1.46 objective (Carl Zeiss), also a LD C-Apochromat 40×/1.1 W Korr UV–VIS-IR objective (Carl Zeiss) was used. Pixel sizes were respectively 22.1 nm and 54.8 nm and image resolution was 512×512. Pixel dwell times (τ_P) of 163.9 μs, 102 μs, 51.8 μs, 25.6 μs and 6.4 μs were used. This range of scan speeds was used to explore possible fast motion of the receptors. The associated line times can be calculated as $1200\tau_P n_{tracks}$, where n_{tracks} is the number of times each line is sequentially scanned before proceeding to the next line. These multiple scanning of each line was applied to increase the line time to further expand the dynamic range of the technique. Image analysis was performed in the MATLAB environment as published elsewhere [59].

2.8. Temporal image correlation spectroscopy

Transfected cells were stained as described and kept at 37 °C through the use of a commercial stage incubator (Pecon GmbH, Erbach, Germany). Cargille type 37 (Cargille Labs, Cedar Grove, NJ, USA) was used as immersion oil. All images were acquired using the setup as described for dSTORM, but without the 405 nm laser light. Two neutral density filters (optical densities 2.5 and 0.1) were introduced to minimize photobleaching of Alexa 488 as much as possible. To reduce the photobleaching even further, a shutter in the beam path, which also triggered the camera, was used to block the laser light between consecutive images. The exposure time of the

camera was kept constant at 50 ms and the EM gain was set at 149. Images were acquired at various acquisition rates ranging from 50 ms to 5 s. Data analysis was performed using custom written software in the MATLAB environment according to published approaches [40,60]. A correction for photobleaching was applied as described [40].

2.9. Single particle tracking

The SPT measurements were carried out on the set-up that also accommodated the dSTORM and TICS measurements [61]. Alexa 647 was used with excitation from a 60 mW 642 nm diode laser (Excelsior 642, Spectra-Physics), a z647rdc DC and a 665LP emission filter (Chroma). The exposure time of the camera was kept constant at 50 ms and the EM gain was set at 610. Bottom membrane images were acquired at 10 Hz with shuttered exposure to minimize photobleaching. Live cells were kept at 37 °C through the use of a commercial stage incubator (Pecon) and Cargille type 37 was used as immersion oil. Particle detection and localization, trajectory construction and calculation of the mean square displacements ($\langle r^2 \rangle$) for each time lag (t_{lag}) were done by in-house developed MATLAB® routines. Only trajectories with a minimum of 16 time steps were considered. The localization precision (σ), determined by tracking of Alexa 647 labeled GlyRs at 37 °C in cell membranes fixed for 10 min with 4% PFA, was kept fixed. For short time range diffusion, the diffusion coefficient was determined by fitting the first three time lags (D_{1-3}) of trajectories with the linear function $r^2 = 4Dt_{lag} + 4\sigma^2$ [62]. For long time range diffusion, fitting of the first quarter [62] of the displacement data was done using the non-linear function $r^2 = 4D't_{lag}^{\alpha} + 4\sigma^2$ [30,63], with D′ and α as freely adjustable fitting parameters. The α-exponent allows for a time-dependent diffusion coefficient (D′), which improved fitting significantly. Tracks were considered immobile if the $\langle r^2 \rangle_{t_{lag}} < 4\sigma^2$ for any time lags in the fit or if $\langle r^2 \rangle_{t_{lag}=1} > \langle r^2 \rangle_{t_{lag}>1}$.

3. Results

Each experimental technique was applied to two separate expression systems. Each system comprised the expression of a different α3 (K or L) subunit isoform in HEK 293 cells. For both isoforms individual expression of the subunit leads to the formation of functional transmembrane receptors. This was verified by analyzing protein expression with western blot and measuring glycine-evoked membrane currents using whole-cell patch-clamp (Supplementary material 2).

3.1. GlyR α3 aggregation state

The membrane aggregation state of the GlyR α3 isoforms in fixed samples was studied by using ICS and dSTORM. ICS analysis was carried out on regions of the bottom membrane with an apparent homogeneous distribution of fluorescent entities (Fig. 2). The average brightness (counts/s per entity) was determined by combining the measured average density of fluorescent entities together with the associated average fluorescence intensity of the image (Table 1) [37]. Using this analysis, the fluorescent entities of GlyR α3L are found to be approximately 8 times (7.5 ± 0.4) brighter as compared to their GlyR α3K counterparts. Assuming that the brightness of the fluorescent labels is independent of the aggregation state of the receptor and that each fluorescent entity of GlyR α3K corresponds to an individual receptor, it can be concluded that each fluorescent entity of GlyR α3L corresponds with a cluster comprising eight times more labeled receptors. The size of the GlyR α3L clusters is below the diffraction limit as the observed radial beam radius ω_0 is essentially constant (Table 1).

dSTORM experiments yield point accumulation images representing a map of GlyR α3 locations in the bottom membrane (Fig. 3a,b). Analysis of these point locations by Ripley's H-function indicates a clear deviation from random distribution for the GlyR α3L, and this in contrast to the GlyR α3K. The GlyR α3L point distribution yields positive values for the H-function, up to 1 μm and with the maximum of the H-function at 280 nm. For the GlyR α3K the maximum of the H-function is at a distance of ≈20 nm, which is of the same order as the localization precision.

3.2. Study of GlyR α3 diffusion using ensemble techniques

FRAP experiments analyzed using the uniform disk model and the new reference method yielded a diffusion coefficient of 0.15 ± 0.01 μm²/s with a mobile fraction of 0.93 ± 0.04 for the GlyR α3K (Fig. 4a). Variations in ROI size did not reveal changes in diffusion coefficient (Fig. 4c) nor in mobile fraction (data not shown). Unfortunately, due to the low density of the bright clusters from GlyR α3L, applying FRAP to this isoform was unsuccessful (Fig. 4b). Movement of these bright clusters in and out of the bleach region dramatically affects the recovery curve and renders it unsuitable for further analysis.

Analysis of diffusion measurements carried out with RICS reveals a difference in diffusion coefficient of more than an order of magnitude between GlyRs α3K and α3L (respectively 0.11 ± 0.02 μm²/s and 0.008 ± 0.002 μm²/s). Coarse spatial mapping of receptor diffusion in the bottom membrane, displays variations that are relatively small compared to the inter-isoform difference (Fig. 5a,b). Application of several scan speeds confirmed that no faster moving fraction of both types of receptors existed.

TICS experiments performed on GlyRs α3K and α3L revealed that both splice variants contain two species of receptor diffusion (Fig. 6). Due to bleaching and the limitations of the photobleaching correction (Supplementary material 3), only the diffusion of the fastest species could be reliably characterized. The average values across the experiments for these species are 0.16 ± 0.07 μm²/s for the GlyR α3K and 0.021 ± 0.009 μm²/s for the GlyR α3L. In summary, all ensemble techniques yield similar diffusion coefficients for each individual isoform (Table 2).

3.3. Study of the GlyR α3 diffusion using single particle tracking

The diffusing GlyR α3 isoforms were monitored by tracking individual fluorescent features in the bottom membrane (Fig. 7a,b). The obtained distribution for short time range D_{1-3} is shifted towards faster diffusion for the GlyR α3K compared to the GlyR α3L, with respective averages of 0.13 μm²/s and 0.044 μm²/s (Fig. 7c). For longer time ranges, a time-dependent diffusion coefficient better suited the data. This implied that the average α-exponents were indicative of anomalous diffusion ($\alpha \neq 1$), equaling 0.87 for the GlyR α3K and 0.73 for the GlyR α3L. The α-exponents exhibit a broad distribution due to imperfect sampling [29]. Nevertheless a clear distinction can be made between GlyRs α3K and α3L. The distribution of the former has a zero skewness centered on normal diffusion ($\alpha = 1$), yet contains more weight on anomalous subdiffusion ($\alpha < 1$) (Fig. 7d). The distribution of the latter has positive non-zero skewness, with the center on anomalous subdiffusion and with a long tail to the right suggesting the presence of anomalous superdiffusion ($\alpha > 1$) (Fig. 7d). For both receptor types a fraction of the analyzed trajectories was designated as immobile within the time-dependent diffusion model approach. This concerned 5% of the trajectories for the GlyR α3K and 15% for the GlyR α3L (Table 3).

Upon inspection of single trajectories, it can be ascertained that transient trapping is present for particles displaying tracks with anomalous subdiffusion (Fig. 8a,b). This was observed for both α3K and α3L receptors. On the other hand, tracks corresponding with anomalous superdiffusion reflect clear directed motion combined with local trapping (Fig. 8c,d). The latter type of complex particle motion was only observed for the GlyR α3L.

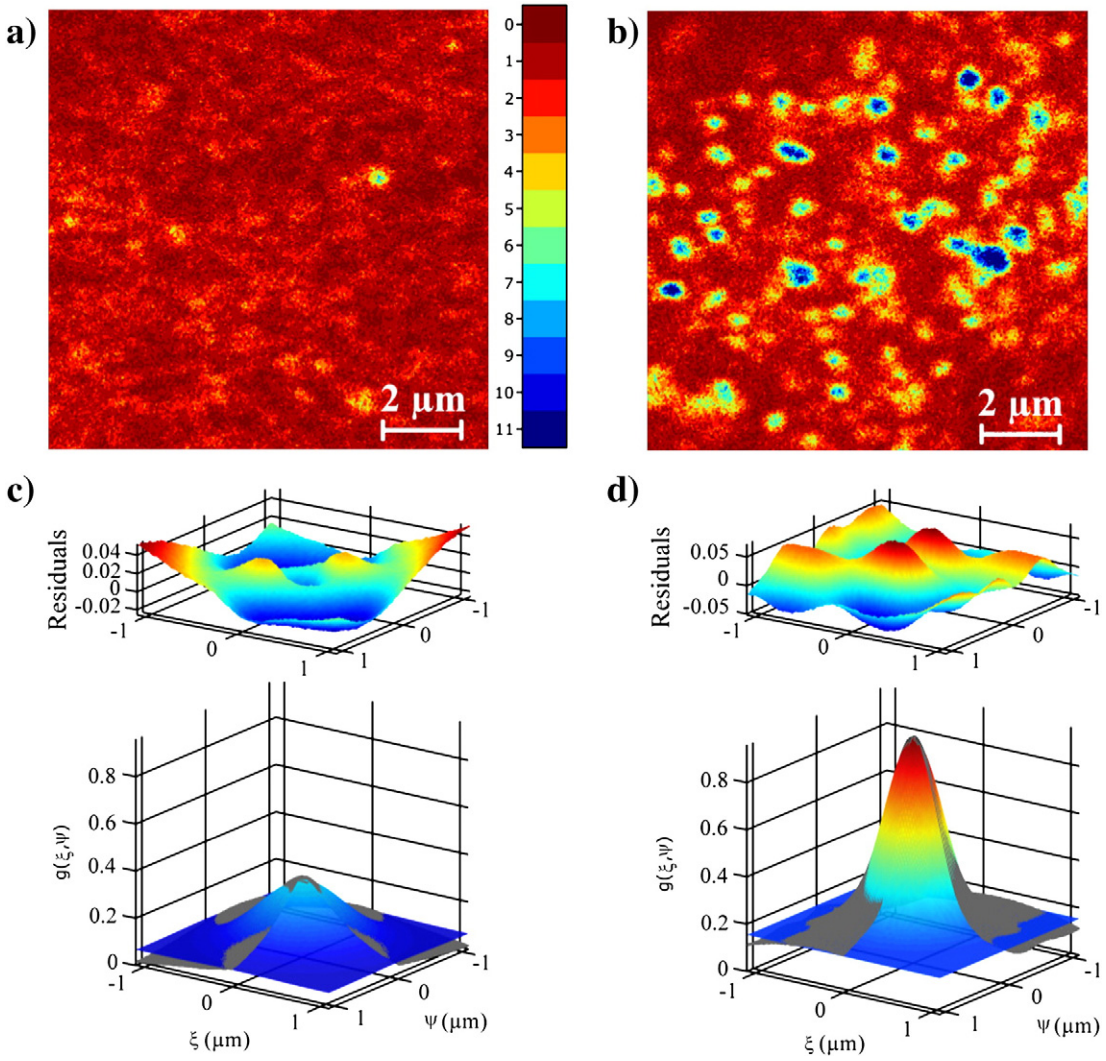

Fig. 2. Representative images obtained from respectively GlyRs α3K and α3L in fixed HEK 293 cells are shown by (a) and (b). Both images have the same intensity scale. Qualitative inspection reveals a diffuse staining of the K splice variant and a punctate pattern of GlyR α3L. (c) and (d) are the experimentally obtained spatial autocorrelation function (gray shade, facing quadrant removed) of respectively GlyRs α3K and α3L, together with the best fit (colored surface). The plot of the weighted residuals is indicated above the corresponding spatial autocorrelation function.

4. Discussion

In this study, differential diffusion and aggregation of the homomeric GlyR α3 related to the isoform composition were investigated. The difference in aggregation states of the GlyR isoforms α3K and α3L was confirmed using ICS and dSTORM. The differences in receptor diffusion were studied with a variety of fluorimetric techniques. Further discussion pertains to the integrated view of receptor diffusion achieved by combining ensemble and single particle fluorimetric techniques. Finally, the results are placed in a physiological context and the perspectives for further study of the GlyR α3 are outlined.

4.1. The GlyR α3 isoforms differ in aggregation state

The difference between the diffuse staining pattern of GlyR α3K and the punctate staining pattern of GlyR α3L is obvious, even through regular microscopic observation. This differential staining pattern reflects the different aggregation state of both receptor isoforms. Eichler et al. estimated the cluster size of GlyR α3L in transfected primary hippocampal neurons, but the number of receptors per cluster could not be determined [17]. In order to estimate this number and to enable the detection of even smaller differences in aggregation state, the application of ICS and dSTORM to the current expression systems was explored. Both methods start from a static snapshot of the cellular model obtained through chemical fixation.

The ICS results revealed that each GlyR α3L cluster comprised an average of 8 labeled receptors assuming the exclusive presence of individual receptors for GlyR α3K and a constant brightness per receptor. When aggregation reduces this brightness, as could well occur by steric hindrance of bound antibody, 8 will be a lower limit. Furthermore, the size of the detected GlyR α3L clusters was still below the diffraction limit, as indicated by the lack of increment of

Table 1
ICS analysis performed on fixed cells expressing either GlyR α3K or GlyR α3L. Particle density and brightness were corrected for background intensity and non-specific binding of the antibody.

Splice variant[a]	Density (entities/µm^2)	Brightness (counts/s entity)	ω_0 (nm)
GlyR α3K	5.9 ± 0.8[b]	0.28 ± 0.04	43 × 10 ± 8 × 10
GlyR α3L	1.3 ± 0.3	2.1 ± 0.4	40 × 10 ± 2 × 10

[a] For each isoform 9 cells were measured.
[b] Errors are reported as standard error of the mean.

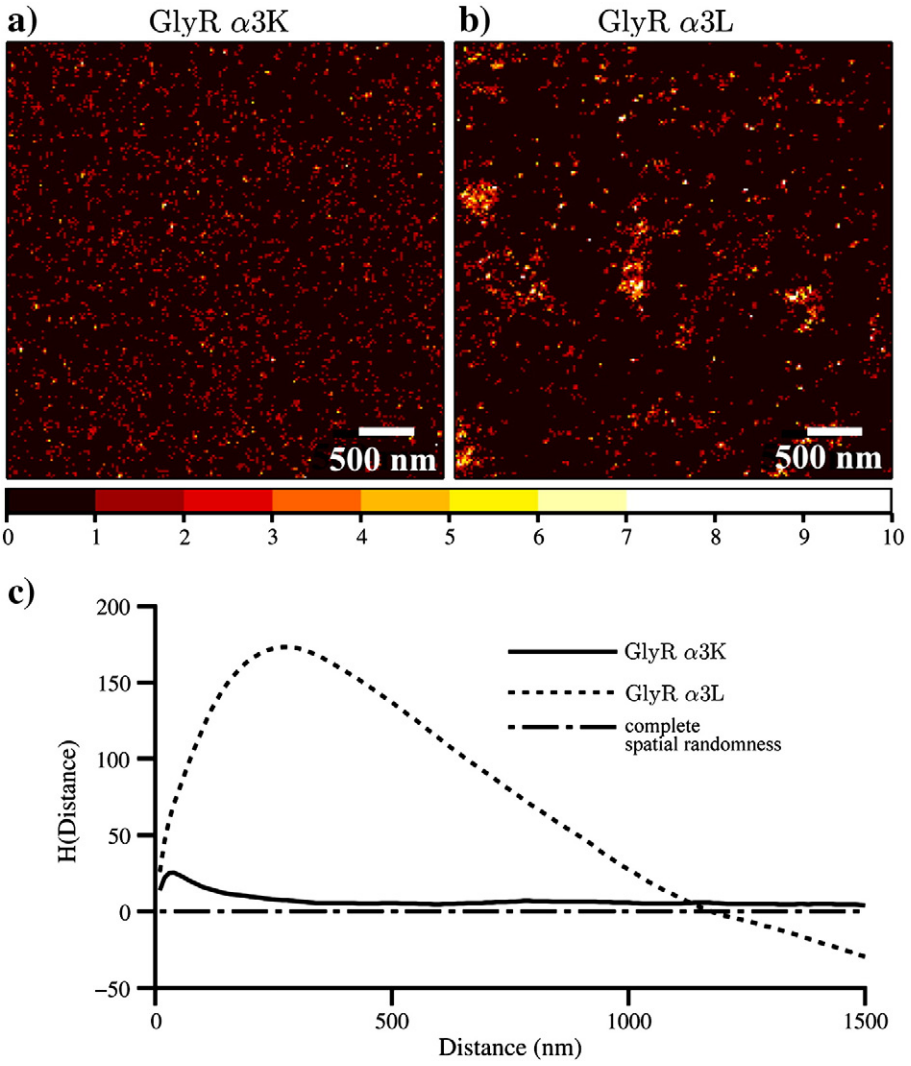

Fig. 3. Representative accumulated point map images obtained from respectively the GlyR α3K (a) and the GlyR α3L (b) in fixed HEK 293 cells using dSTORM. Both images have the same intensity scale. Ripley's multi-distance spatial clustering analysis (c) reveals profound clustering of the GlyR α3L compared to the GlyR α3K.

the average observation profile radius ω_0 retrieved in ICS (Table 1). This is consistent with the estimated number of labeled receptors in combination with the size of the GlyR, which should be close to the published 8.5 nm radial diameter of the structurally related nicotinic acetylcholine receptor [64,65].

In addition to the diffraction-limited ICS, the super-resolution method dSTORM was applied to obtain sub-diffraction resolution images of the receptors. Analysis of these data using Ripley's H-function indicates a clear difference in aggregation state between the isoforms. While the GlyR α3L displays a non-uniform clustering distribution, any clustering seen with the GlyR α3K is minimal and barely exceeds artifacts generated by the repeated localization of identical particles [66]. The maximum of Ripley's H-function cannot be used as a rigorous estimate of the mean cluster size as this maximum depends on the cluster separation [67]. Also, a distribution of cluster sizes cannot be excluded and the higher number of detected events for larger clusters can introduce a bias.

4.2. GlyR α3 diffusion studied by ensemble techniques

The diffusion of GlyR α3K was successfully studied by FRAP. Two models for free diffusion, which differ in their assumption of the shape of the bleaching beam, were cautiously applied. It is known that a model for free diffusion might yield incorrect results in the presence of anomalous diffusion while apparently being correct based on the quality of the fit [68]. However, the low immobile fraction observed by both models in the experiments reflects the suitability of the free diffusion model and suggests that the motion of the GlyR α3K receptors is close to that of free diffusion. Furthermore, for receptors undergoing anomalous diffusion, the immobile fraction would be much higher upon analysis with a constant diffusion coefficient. Finally, the lack of dependency of both D and the immobile fraction on the ROI size are also indicative for the absence or limited contribution of anomalous diffusion. The results of both models did not differ significantly.

Unfortunately, GlyR α3L could not be studied by FRAP due to the presence of clusters. Movement of clusters in and out the ROI dramatically affects the fluorescence intensity inside the ROI. A similar effect is seen when the concentration of fluorophores is too low [69].

While RICS in a biological context is mainly used to measure the diffusion of proteins in the cytoplasm [38,70], this technique has been previously used by us to characterize diffusion of membrane components [59,71]. The low diffusion coefficients of membrane proteins force the application of low scan speeds near the limit of the capabilities of our CLSM set-up. Coarse spatial mapping achieved with RICS revealed a limited spatial dependency of the diffusion coefficient for each individual isoform over the cell surface [39,59]. In contrast to FRAP, RICS was able to measure the diffusion coefficient of both

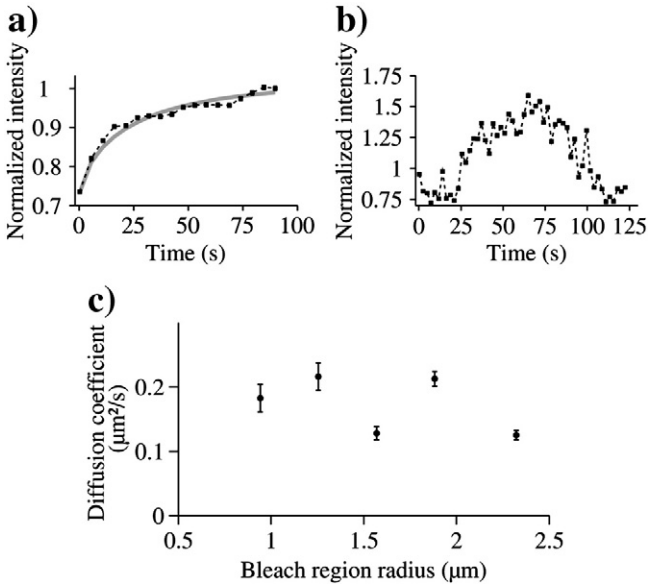

Fig. 4. Representative fluorescence recovery from respectively GlyRs α3K and α3L expressed in HEK 293 cells are shown by (a) and (b). For the GlyR α3K, the model properly fit the curve, while fitting the recovery curve of GlyR α3L was unsuccessful. Diffusion coefficients for the GlyR α3K obtained from 31 cells and analyzed using the uniform disk model are plotted as the average and standard deviation per ROI radius (c). The overall average of the diffusion coefficient is $0.15 \pm 0.01\ \mu m^2/s$ and of the mobile fraction is 0.93 ± 0.04.

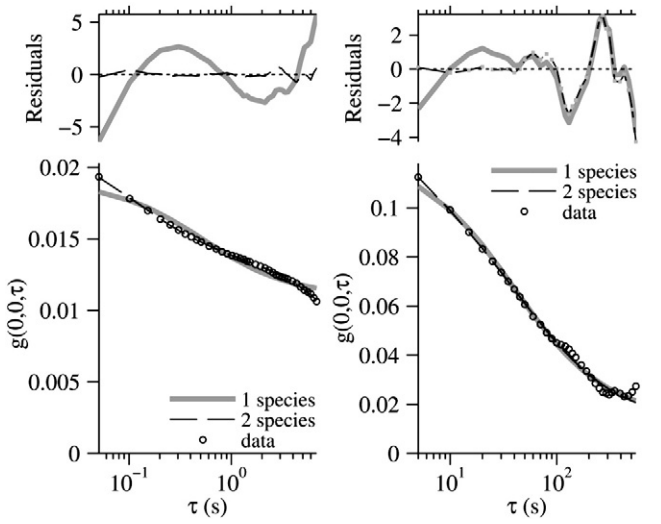

Fig. 6. The temporal autocorrelation function obtained in TICS analysis of GlyRs α3K (a) and α3L (b) are plotted, together with the 1 species and 2 species fit. The upper panels show the weighted residuals.

isoforms, with a good agreement for both techniques for the K isoform. The difference in magnitude of the obtained diffusion coefficients of both isoforms is larger than expected based on their difference in aggregation state estimated with ICS and dSTORM. This provides evidence for an influence, not inherent to the receptors, such as the membrane constitution or submembranous structures.

TICS was originally applied on a CLSM [40], but the available frame rate would not allow to resolve the large, fast moving fractions of the proteins. Therefore, we used a TIRFM with a frame rate optimized for the time scale of the expected kinetics. From simulated data (Supplementary material 3), it is shown that for the observed bleaching rate, the experimental data can be corrected appropriately so that reliable estimates for the diffusion coefficient of the fastest species can be obtained. The use of TICS revealed the presence of an apparent slower diffusing species, but due to the bleaching rate this information could not unambiguously be interpreted.

4.3. SPT reveals anomalous diffusion in GlyR α3 diffusion

The short time range D_{1-3} derived from SPT confirms faster diffusion for the GlyR α3K in comparison to the GlyR α3L. This could be explained by cluster formation of α3L receptors, as seen by ICS and dSTORM, resulting in large complexes exhibiting slow but normal membrane diffusion. However, the observation that for a longer time range the diffusion coefficient becomes time-dependent, suggests that a larger hydrodynamic radius due to clustering of the GlyR α3L cannot be the only determining factor. The average of the α-exponents ($\alpha < 1$) indicates that both receptor isoforms undergo subdiffusion. The fact that this is more pronounced for the GlyR α3L, which also displays a larger immobile fraction and a higher degree of clustering, supports the idea of local transient trapping of receptors in small regions [72,73]. This can be qualitatively confirmed by visual inspection of the GlyR α3L tracks. A lower degree of subdiffusion for the GlyR α3K could indicate that these receptors are transiently trapped in larger regions. However, the size and the distribution of these regions have to be consistent with the nearly uniform distribution of the GlyR α3K observed with dSTORM. An alternative assumption is that the α3K isoform is less prone to trapping and therefore resides less in the trapped state. A higher degree of interaction determining the motion of GlyR α3L is corroborated by the

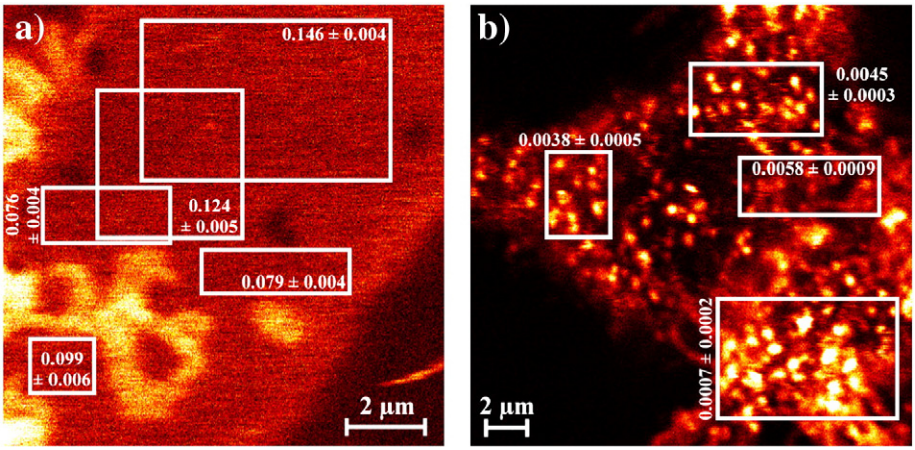

Fig. 5. RICS of live HEK 293 cells expressing GlyRs α3K (a) and α3L (b) allows for a coarse mapping of the mobility of the respective receptors. Each white rectangular box represents an analyzed area with the obtained diffusion coefficient [in $\mu m^2/s$] and standard error reported. In general, there was a difference of over one decade between the diffusion coefficients of both splice variants. In addition, there was also variation of the diffusion coefficient within a single cell, albeit to a lesser extent. An identical color map was applied for both images.

Table 2
The average diffusion coefficient (in $\mu m^2/s$) as obtained per ensemble microfluorimetric technique.

Splice variant	FRAP	RICS	TICS
GlyR α3K[a]	0.15 ± 0.01[c]	0.11 ± 0.02	0.16 ± 0.07
GlyR α3L[b]	Not feasible	0.008 ± 0.002	0.021 ± 0.009

[a] Cells analyzed per technique. FRAP: 31, RICS: 6, TICS: 6.
[b] Cells analyzed per technique. FRAP: 0, RICS: 6, TICS: 6.
[c] Errors are represented as standard error of the mean.

presence of anomalous superdiffusion [74] in the receptor motion. The combination of trapping and superdiffusion, as found in the trajectories of the GlyR α3L, is likely to represent receptors actively being transported from, to or between different locations in the membrane.

4.4. An integrated view of receptor diffusion

Given the spatio-temporal properties of the GlyR α3 diffusion, SPT allowed for the most detailed characterization. However, the possible presence of bias inherent to SPT or the application of SPT to live cells warrants a combination with ensemble techniques. The first aspect is that highly mobile particles are more difficult to track compared to their slower moving counterparts, meaning a possible bias towards types of subdiffusion can be present. Upon observation of subdiffusion, as for the GlyR α3, a comparison with FRAP experiments is of importance, to estimate the relevance on the cellular level. In the instance of the GlyR α3K this revealed a minimal impact of the subdiffusion measured by SPT, on large scale receptor motion measured with FRAP [68]. Second, due to the bleaching of the particles, a bias towards fresh molecules diffusing into the bottom membrane from outside the measurement plane can arise. A comparison of the diffusion parameters measured with techniques requiring minimal measurement bleaching, such as TICS and FRAP, can resolve whether representative fractions are measured. In our case a good agreement between diffusion coefficients from single molecule tracking (D_{1-3}) and ensemble techniques was found. Moreover, a good agreement between the immobile fractions measured with FRAP and SPT was measured. Furthermore, coarse spatial mapping with RICS confirmed homogeneous diffusion patterns on the cellular level. Third, in choosing cells for SPT measurements, a selection bias can occur towards cells yielding the highest fluorescence signal or containing bright fluorescent entities. Cells showing an overall high level of protein expression after transfection are usually unhealthy [75] and the presence of bright fluorescent entities can bias particle detection parameters. Again, comparing the results obtained with SPT to those obtained with ensemble techniques, where cells are selected based on the ensemble fluorescence signal, decreases the risk of biased sampling. Exemplary is the detection of multiple species with TICS, which confirms that the complex GlyR α3 motion found with SPT is not a technique related artifact.

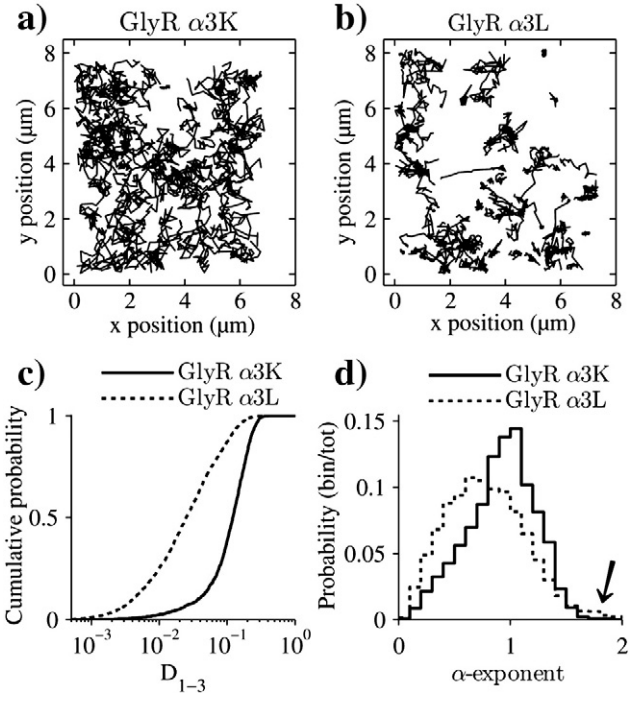

Fig. 7. Representative trajectory plots, shown for the GlyRs α3K (a) and α3L (b). Comparison of the cumulative distributions of short time range D_{1-3} shows faster overall diffusion for the GlyR α3K compared to the GlyR α3L (c). The distribution of α-exponents indicates anomalous subdiffusion in both receptor populations (d). For the GlyR α3L, a subset of tracks also displays anomalous superdiffusion (arrow). (bin = number of elements in bin, tot = total number of elements in distribution).

4.5. Perspectives for the GlyR α3

The diffusion coefficients reported here for the GlyR α3 are within the range expected for proteins diffusing in the cell membrane [76,77]. However, experimental parameters such as the applied cell line, measurement temperature and time of measurement, given their influence on membrane viscosity, thermal agitation, expression level and molecular interactions, are key factors when comparing protein diffusion. Variations in these parameters hamper a comparison with reported values for other GlyR subtypes [78–80]. Nevertheless the results can be placed in a biological context. Receptor diffusion plays an essential role in neuronal function as it allows for renewal of receptors in the desensitized state and regulation of postsynaptic receptor pool size [12,81]. Homomeric GlyR α3K channels were shown to contribute to tonic inhibition of neuronal excitability, which requires receptors in the non-desensitized state [82,18]. Compared with α3L, GlyR α3K desensitizes more rapidly [16] and, therefore, its faster diffusion makes sense as it increases the probability of receptor cycling between endocytic and cell plasma membrane compartments, which will facilitate receptor renewal [12]. Furthermore, this study adds to the understanding of receptor desensitization mechanisms. In fact, it was shown that increased GlyR α1 receptor density in gephyrin-dependent clusters facilitates desensitization, whereas in case of GlyR α3L just the opposite was observed [9,16]. Thus, GlyR clustering is not a universal mechanism of desensitization but also involves receptor conformation depending on primary structure or receptor associated proteins other than gephyrin [83,84].

The next step towards understanding the role of RNA splicing in GlyR α3 function will be the identification of proteins that interact with the RNA splice insert TEAFALEKFYRFSDT located in the large cytosolic loop between transmembrane domains 3 and 4 of GlyR α3L. A similar fluorimetric strategy as formulated here can be used to explore different biological settings. Pharmacological breakdown of the cytoskeleton has been shown to influence GlyR dynamics in cultured neurons [79,80]. Another option is depleting membrane cholesterol, thereby influencing the different types of lipid rafts

Table 3
The average short time range D_{1-3} (in $\mu m^2/s$) is reported for both isoforms. The averages of the free fit parameters (D′, α-exponents) from the non-linear fit of diffusion at longer time range are represented together with the immobile fraction.

SPT	Short time range	Long time range		
Splice variant	D_{1-3}	D′	α-Exponent	Immobile fraction[a]
GlyR α3K[b]	0.129 ± 0.002[c]	0.133 ± 0.003	0.866 ± 0.008	5%
GlyR α3L[d]	0.0436 ± 0.0008	0.042 ± 0.001	0.736 ± 0.006	15%

[a] See Materials and methods for criteria.
[b] Number of cells measured: 7, number of trajectories analyzed: 1629.
[c] Errors are represented as standard error of the mean.
[d] Number of cells measured: 9, number of trajectories analyzed: 4291.

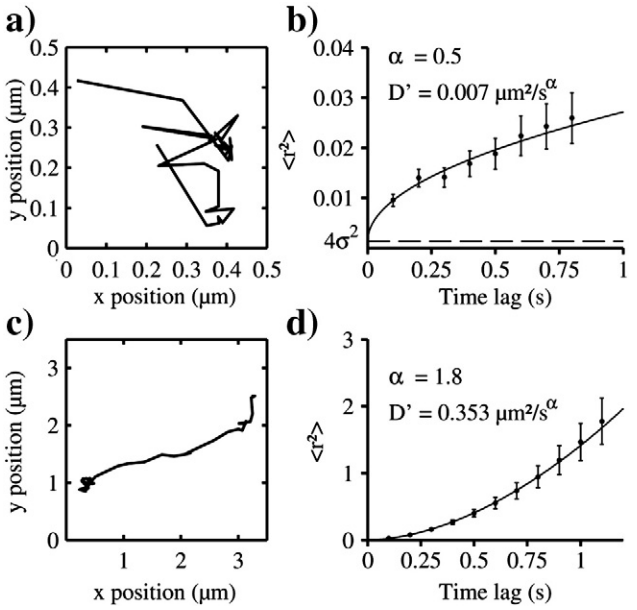

Fig. 8. To interpret the deviation from normal diffusion, representative tracks from particles with anomalous α-exponents are shown (a, c). Particles with an α-exponent<1 exhibit diffusion with transient trapping (a), the localization precision is also represented (dashed line, b). Particles with an α-exponent>1 show a heterogeneous displacement pattern (c), where the proportion of superdiffusion outweighs the subdiffusion (d).

which have been reported in HeLa cells [85]. Disturbance of lipid rafts can lead to dissociation of raft induced protein aggregation and altered protein function [86,87]. An alternative approach for studying GlyR α3 interactions involves site-directed mutagenesis of the insert region. This has previously been applied for studying the regulatory capabilities of the splice insert on channel gating and domain structure [88]. By probing all these conditions, mechanisms determining the GlyR α3 behavior can be better understood.

An appropriate exploratory strategy for examining any transmembrane protein should maximize efficiency in screening multiple conditions and minimize the risk of overlooking any changes in receptor behavior. Therefore labor intensity, applicability and spatio-temporal sampling should be considered when developing a screening approach. This report offers a strong foundation for making these considerations.

Acknowledgements

We would like to thank Ir. Ben De Clercq for providing us with the proper settings of the Becker and Hickl detection system. GlyR expression constructs were obtained thanks to the funding by the Helmholtz Association (VH-NG-246 to J.C.M.). S.R. and J.H. acknowledge financial support of the "Fonds voor Wetenschappelijk Onderzoek FWO" (grants G.0402.09, G.0413.10, G.0697.11), the K. U. Leuven Research Fund (GOA 2011/03), the Flemish government (long-term structural funding: Methusalem funding CASASMETH/08/04). S.R., J.H. and M.A. thank the Federal Science Policy of Belgium (IAP-VI/27). M.A. recognizes the Province of Limburg (Belgium) for the financial support within the tUL IMPULS FASE II program allowing for upgrading the laser source used in this work. The support by the FWO-onderzoeksgemeenschap "Scanning and Wide Field Microscopy of (Bio)-organic Systems" is gratefully acknowledged by J.H. and M.A.

Appendix A. Supplementary data

Supplementary data to this article can be found online at http://dx.doi.org/10.1016/j.bbamem.2012.08.010.

References

[1] L. Groc, L. Bard, D. Choquet, Surface trafficking of N-methyl-D-aspartate receptors: physiological and pathological perspectives, Neuroscience 158 (2009) 4–18.
[2] F.J. Barrantes, Cholesterol effects on nicotinic acetylcholine receptor, J. Neurochem. 103 (Suppl. 1) (2007) 72–80.
[3] I. Chung, R. Akita, R. Vandlen, D. Toomre, J. Schlessinger, I. Mellman, Spatial control of EGF receptor activation by reversible dimerization on living cells, Nature 464 (2010) 783–787.
[4] Z.Q. Xu, X. Zhang, L. Scott, Regulation of G protein-coupled receptor trafficking, Acta Physiol (Oxf.) 190 (2007) 39–45.
[5] D. Lingwood, K. Simons, Lipid rafts as a membrane-organizing principle, Science 327 (2010) 46–50.
[6] K. Ritchie, R. Iino, T. Fujiwara, K. Murase, A. Kusumi, The fence and picket structure of the plasma membrane of live cells as revealed by single molecule techniques (Review), Mol. Membr. Biol. 20 (2003) 13–18.
[7] Y. Sako, A. Kusumi, Compartmentalized structure of the plasma membrane for receptor movements as revealed by a nanometer-level motion analysis, J. Cell Biol. 125 (1994) 1251–1264.
[8] C. Bedet, J.C. Bruusgaard, S. Vergo, L. Groth-Pedersen, S. Eimer, A. Triller, C. Vannier, Regulation of gephyrin assembly and glycine receptor synaptic stability, J. Biol. Chem. 281 (2006) 30046–30056.
[9] P. Legendre, E. Muller, C.I. Badiu, J. Meier, C. Vannier, A. Triller, Desensitization of homomeric alpha1 glycine receptor increases with receptor density, Mol. Pharmacol. 62 (2002) 817–827.
[10] K. Simons, D. Toomre, Lipid rafts and signal transduction, Nat. Rev. Mol. Cell Biol. 1 (2000) 31–39.
[11] J.A. Allen, R.A. Halverson-Tamboli, M.M. Rasenick, Lipid raft microdomains and neurotransmitter signalling, Nat. Rev. Neurosci. 8 (2007) 128–140.
[12] D. Choquet, Fast AMPAR trafficking for a high-frequency synaptic transmission, Eur. J. Neurosci. 32 (2010) 250–260.
[13] H.D. MacGillavry, J.M. Kerr, T.A. Blanpied, Lateral organization of the postsynaptic density, Mol. Cell. Neurosci. 48 (2011) 321–331.
[14] J. Meier, C. Vannier, et al., Fast and reversible trapping of surface glycine receptors by gephyrin, Nature Neuroscience 4 (3) (2001) 253–260.
[15] J. Kuhse, V. Schmieden, H. Betz, Identification and functional expression of a novel ligand binding subunit of the inhibitory glycine receptor, J. Biol. Chem. 265 (1990) 22317–22320.
[16] Z. Nikolic, B. Laube, R.G. Weber, P. Lichter, P. Kioschis, A. Poustka, C. Mulhardt, C.M. Becker, The human glycine receptor subunit alpha3. Glra3 gene structure, chromosomal localization, and functional characterization of alternative transcripts, J. Biol. Chem. 273 (1998) 19708–19714.
[17] S.A. Eichler, B. Forstera, B. Smolinsky, R. Juttner, T.N. Lehmann, M. Fahling, G. Schwarz, P. Legendre, J.C. Meier, Splice-specific roles of glycine receptor alpha3 in the hippocampus, Eur. J. Neurosci. 30 (2009) 1077–1091.
[18] S.A. Eichler, S. Kirischuk, R. Juttner, P.K. Schafermeier, P. Legendre, T.N. Lehmann, T. Gloveli, R. Grantyn, J.C. Meier, Glycinergic tonic inhibition of hippocampal neurons with depolarizing GABAergic transmission elicits histopathological signs of temporal lobe epilepsy, J. Cell. Mol. Med. 12 (2008) 2848–2866.
[19] P. Legendre, B. Forstera, R. Juttner, J.C. Meier, Glycine receptors caught between genome and proteome — functional implications of RNA editing and splicing, Front. Mol. Neurosci. 2 (2009) 23.
[20] J.W. Lynch, Native glycine receptor subtypes and their physiological roles, Neuropharmacology 56 (2009) 303–309.
[21] D. Axelrod, D.E. Koppel, J. Schlessinger, E. Elson, W.W. Webb, Mobility measurement by analysis of fluorescence photobleaching recovery kinetics, Biophys. J. 16 (1976) 1055–1069.
[22] N. Smisdom, K. Braeckmans, H. Deschout, M. vandeVen, J.-M. Rigo, S.C. De Smedt, M. Ameloot, Fluorescence recovery after photobleaching on the confocal laser-scanning microscope: generalized model without restriction on the size of the photobleached disk, J. Biomed. Opt. 16 (2011) 046021–046028.
[23] D. Alcor, G. Gouzer, A. Triller, Single-particle tracking methods for the study of membrane receptors dynamics, Eur. J. Neurosci. 30 (2009) 987–997.
[24] C.M. Anderson, G.N. Georgiou, I.E. Morrison, G.V. Stevenson, R.J. Cherry, Tracking of cell surface receptors by fluorescence digital imaging microscopy using a charge-coupled device camera. Low-density lipoprotein and influenza virus receptor mobility at 4 degrees C, J. Cell Sci. 101 (Pt 2) (1992) 415–425.
[25] S. Wieser, G.J. Schutz, Tracking single molecules in the live cell plasma membrane-Do's and Don't's, Methods 46 (2008) 131–140.
[26] K. Peneva, G. Mihov, F. Nolde, S. Rocha, J. Hotta, K. Braeckmans, J. Hofkens, H. Uji-i, A. Herrmann, K. Mullen, Water-soluble monofunctional perylene and terrylene dyes: powerful labels for single-enzyme tracking, Angew. Chem. Int. Ed. Engl. 47 (2008) 3372–3375.
[27] S. Rocha, J.A. Hutchison, K. Peneva, A. Herrmann, K. Mullen, M. Skjot, C.I. Jorgensen, A. Svendsen, F.C. De Schryver, J. Hofkens, H. Uji-i, Linking phospholipase mobility to activity by single-molecule wide-field microscopy, Chemphyschem 10 (2009) 151–161.
[28] Q. Tang, M. Edidin, Lowering the barriers to random walks on the cell surface, Biophys. J. 84 (2003) 400–407.
[29] H. Qian, M.P. Sheetz, E.L. Elson, Single particle tracking. Analysis of diffusion and flow in two-dimensional systems, Biophys. J. 60 (1991) 910–921.
[30] T.J. Feder, I. BrustMascher, J.P. Slattery, B. Baird, W.W. Webb, Constrained diffusion or immobile fraction on cell surfaces: a new interpretation, Biophys. J. 70 (1996) 2767–2773.
[31] S.W. Paddock, Confocal laser scanning microscopy, Biotechniques 27 (1999) 992–996 (998-1002, 1004).

[32] W.B. Amos, J.G. White, How the confocal laser scanning microscope entered biological research, Biol. Cell 95 (2003) 335–342.
[33] D. Axelrod, Total internal reflection fluorescence microscopy in cell biology, Traffic 2 (2001) 764–774.
[34] N.L. Thompson, J.K. Pero, Total internal reflection fluorescence microscopy: applications in biophysics, in: M. Hof, R. Hutterer, V. Fidler (Eds.), Fluorescence Spectroscopy in Biology, vol. 3, Springer, Berlin Heidelberg, 2005, pp. 79–103.
[35] S.M. Simon, Partial internal reflections on total internal reflection fluorescent microscopy, Trends Cell Biol. 19 (2009) 661–668.
[36] N.O. Petersen, P.L. Hoddelius, P.W. Wiseman, O. Seger, K.E. Magnusson, Quantitation of membrane receptor distributions by image correlation spectroscopy: concept and application, Biophys. J. 65 (1993) 1135–1146.
[37] P.W. Wiseman, N.O. Petersen, Image correlation spectroscopy. II. Optimization for ultrasensitive detection of preexisting platelet-derived growth factor-beta receptor oligomers on intact cells, Biophys. J. 76 (1999) 963–977.
[38] C.M. Brown, R.B. Dalal, B. Hebert, M.A. Digman, A.R. Horwitz, E. Gratton, Raster image correlation spectroscopy (RICS) for measuring fast protein dynamics and concentrations with a commercial laser scanning confocal microscope, J. Microsc. 229 (2008) 78–91.
[39] M.J. Rossow, J.M. Sasaki, M.A. Digman, E. Gratton, Raster image correlation spectroscopy in live cells, Nat. Protoc. 5 (2010) 1761–1774.
[40] D.L. Kolin, S. Costantino, P.W. Wiseman, Sampling effects, noise, and photobleaching in temporal image correlation spectroscopy, Biophys. J. 90 (2006) 628–639.
[41] J. Sankaran, M. Manna, L. Guo, R. Kraut, T. Wohland, Diffusion, transport, and cell membrane organization investigated by imaging fluorescence cross-correlation spectroscopy, Biophys. J. 97 (2009) 2630–2639.
[42] E. Betzig, G.H. Patterson, R. Sougrat, O.W. Lindwasser, S. Olenych, J.S. Bonifacino, M.W. Davidson, J. Lippincott-Schwartz, H.F. Hess, Imaging intracellular fluorescent proteins at nanometer resolution, Science 313 (2006) 1642–1645.
[43] C. Flors, J. Hotta, H. Uji-i, P. Dedecker, R. Ando, H. Mizuno, A. Miyawaki, J. Hofkens, A stroboscopic approach for fast photoactivation–localization microscopy with Dronpa mutants, J. Am. Chem. Soc. 129 (2007) 13970–13977.
[44] S.T. Hess, T.P. Girirajan, M.D. Mason, Ultra-high resolution imaging by fluorescence photoactivation localization microscopy, Biophys. J. 91 (2006) 4258–4272.
[45] M.B. Roeffaers, G. De Cremer, J. Libeert, R. Ameloot, P. Dedecker, A.J. Bons, M. Buckins, J.A. Martens, B.F. Sels, D.E. De Vos, J. Hofkens, Super-resolution reactivity mapping of nanostructured catalyst particles, Angew. Chem. Int. Ed. Engl. 48 (2009) 9285–9289.
[46] M.J. Rust, M. Bates, X.W. Zhuang, Sub-diffraction-limit imaging by stochastic optical reconstruction microscopy (STORM), Nat. Methods 3 (2006) 793–795.
[47] M. Heilemann, S. van de Linde, A. Mukherjee, M. Sauer, Super-resolution imaging with small organic fluorophores, Angew. Chem. Int. Ed. Engl. 48 (2009) 6903–6908.
[48] M. Heilemann, S. van de Linde, M. Schuttpelz, R. Kasper, B. Seefeldt, A. Mukherjee, P. Tinnefeld, M. Sauer, Subdiffraction–resolution fluorescence imaging with conventional fluorescent probes, Angew. Chem. Int. Ed. Engl. 47 (2008) 6172–6176.
[49] S. van de Linde, A. Loschberger, T. Klein, M. Heidbreder, S. Wolter, M. Heilemann, M. Sauer, Direct stochastic optical reconstruction microscopy with standard fluorescent probes, Nat. Protoc. 6 (2011) 991–1009.
[50] S. van de Linde, I. Krstic, T. Prisner, S. Doose, M. Heilemann, M. Sauer, Photoinduced formation of reversible dye radicals and their impact on super-resolution imaging, Photochem. Photobiol. Sci. 10 (2011) 499–506.
[51] K.I. Mortensen, L.S. Churchman, J.A. Spudich, H. Flyvbjerg, Optimized localization analysis for single-molecule tracking and super-resolution microscopy, Nat. Methods 7 (2010) 377–381.
[52] R.E. Thompson, D.R. Larson, W.W. Webb, Precise nanometer localization analysis for individual fluorescent probes, Biophys. J. 82 (2002) 2775–2783.
[53] M. Ehrlich, W. Boll, A. van Oijen, R. Hariharan, K. Chandran, M.L. Nibert, T. Kirchhausen, Endocytosis by random initiation and stabilization of clathrin-coated pits, Cell 118 (2004) 591–605.
[54] B.D. Ripley, 2nd-order analysis of stationary point processes, J. Appl. Probab. 13 (1976) 255–266.
[55] B.D. Ripley, Modeling spatial patterns, J. Roy. Stat. Soc. B Met. 39 (1977) 172–212.
[56] R.D. Phair, S.A. Gorski, T. Misteli, Measurement of dynamic protein binding to chromatin in vivo, using photobleaching microscopy, Methods Enzymol. 375 (2004) 393–414.
[57] R.D. Phair, T. Misteli, High mobility of proteins in the mammalian cell nucleus, Nature 404 (2000) 604–609.
[58] K. Braeckmans, L. Peeters, N.N. Sanders, S.C. De Smedt, J. Demeester, Three-dimensional fluorescence recovery after photobleaching with the confocal scanning laser microscope, Biophys. J. 85 (2003) 2240–2252.
[59] E. Gielen, N. Smisdom, M. vandeVen, B. De Clercq, E. Gratton, M. Digman, J.M. Rigo, J. Hofkens, Y. Engelborghs, M. Ameloot, Measuring diffusion of lipid-like probes in artificial and natural membranes by raster image correlation spectroscopy (RICS): use of a commercial laser-scanning microscope with analog detection, Langmuir 25 (2009) 5209–5218.
[60] J. Sankaran, X. Shi, L.Y. Ho, E.H. Stelzer, T. Wohland, ImFCS: a software for imaging FCS data analysis and visualization, Opt. Express 18 (2010) 25468–25481.
[61] T.Y. Kim, H. Uji-i, M. Moller, B. Muls, J. Hofkens, U. Alexiev, Monitoring the interaction of a single G-protein key binding site with rhodopsin disk membranes upon light activation, Biochemistry 48 (2009) 3801–3803.
[62] M.J. Saxton, Single-particle tracking: the distribution of diffusion coefficients, Biophys. J. 72 (1997) 1744–1753.
[63] P.R. Smith, I.E. Morrison, K.M. Wilson, N. Fernandez, R.J. Cherry, Anomalous diffusion of major histocompatibility complex class I molecules on HeLa cells determined by single particle tracking, Biophys. J. 76 (1999) 3331–3344.
[64] N. Unwin, Refined structure of the nicotinic acetylcholine receptor at 4A resolution, J. Mol. Biol. 346 (2005) 967–989.
[65] J. Kistler, R.M. Stroud, M.W. Klymkowsky, R.A. Lalancette, R.H. Fairclough, Structure and function of an acetylcholine receptor, Biophys. J. 37 (1982) 371–383.
[66] P. Annibale, S. Vanni, M. Scarselli, U. Rothlisberger, A. Radenovic, Identification of clustering artifacts in photoactivated localization microscopy, Nat. Methods 8 (2011) 527–528.
[67] M.A. Kiskowski, J.F. Hancock, A.K. Kenworthy, On the use of Ripley's K-function and its derivatives to analyze domain size, Biophys. J. 97 (2009) 1095–1103.
[68] J.F. Nagle, Long tail kinetics in biophysics? Biophys. J. 63 (1992) 366–370.
[69] D.E. Wolf, Designing, building, and using a fluorescence recovery after photobleaching instrument, Methods Cell Biol. 30 (1989) 271–306.
[70] M.A. Digman, C.M. Brown, P. Sengupta, P.W. Wiseman, A.R. Horwitz, E. Gratton, Measuring fast dynamics in solutions and cells with a laser scanning microscope, Biophys. J. 89 (2005) 1317–1327.
[71] E. Gielen, N. Smisdom, B. De Clercq, M. Vandeven, R. Gijsbers, Z. Debyser, J.M. Rigo, J. Hofkens, Y. Engelborghs, M. Ameloot, Diffusion of myelin oligodendrocyte glycoprotein in living OLN-93 cells investigated by raster-scanning image correlation spectroscopy (RICS), J. Fluoresc. 18 (2008) 813–819.
[72] M.J. Saxton, Single-particle tracking: effects of corrals, Biophys. J. 69 (1995) 389–398.
[73] R. Simson, E.D. Sheets, K. Jacobson, Detection of temporary lateral confinement of membrane proteins using single-particle tracking analysis, Biophys. J. 69 (1995) 989–993.
[74] K.M. Wilson, I.E.G. Morrison, P.R. Smith, N. Fernandez, R.J. Cherry, Single particle tracking of cell-surface HLA-DR molecules using R-phycoerythrin labeled monoclonal antibodies and fluorescence digital imaging, J. Cell Sci. 109 (1996) 2101–2109.
[75] P. Thomas, T.G. Smart, HEK293 cell line: a vehicle for the expression of recombinant proteins, J. Pharmacol. Toxicol. Methods 51 (2005) 187–200.
[76] A. Kusumi, C. Nakada, K. Ritchie, K. Murase, K. Suzuki, H. Murakoshi, R.S. Kasai, J. Kondo, T. Fujiwara, Paradigm shift of the plasma membrane concept from the two-dimensional continuum fluid to the partitioned fluid: high-speed single-molecule tracking of membrane molecules, Annu. Rev. Biophys. Biomol. Struct. 34 (2005) 351–378.
[77] Y. Gambin, R. Lopez-Esparza, M. Reffay, E. Sierecki, N.S. Gov, M. Genest, R.S. Hodges, W. Urbach, Lateral mobility of proteins in liquid membranes revisited, Proc. Natl. Acad. Sci. U.S.A. 103 (2006) 2098–2102.
[78] M. Dahan, S. Levi, C. Luccardini, P. Rostaing, B. Riveau, A. Triller, Diffusion dynamics of glycine receptors revealed by single-quantum dot tracking, Science 302 (2003) 442–445.
[79] M.V. Ehrensperger, C. Hanus, C. Vannier, A. Triller, M. Dahan, Multiple association states between glycine receptors and gephyrin identified by SPT analysis, Biophys. J. 92 (2007) 3706–3718.
[80] C. Charrier, M.V. Ehrensperger, M. Dahan, S. Levi, A. Triller, Cytoskeleton regulation of glycine receptor number at synapses and diffusion in the plasma membrane, J. Neurosci. 26 (2006) 8502–8511.
[81] M.D. Ehlers, M. Heine, L. Groc, M.C. Lee, D. Choquet, Diffusional trapping of GluR1 AMPA receptors by input-specific synaptic activity, Neuron 54 (2007) 447–460.
[82] J.C. Meier, C. Henneberger, I. Melnick, C. Racca, R.J. Harvey, U. Heinemann, V. Schmieden, R. Grantyn, RNA editing produces glycine receptor alpha3(P185L), resulting in high agonist potency, Nat. Neurosci. 8 (2005) 736–744.
[83] H.G. Breitinger, C.M. Becker, The inhibitory glycine receptor-simple views of a complicated channel, Chembiochem 3 (2002) 1042–1052.
[84] P. Legendre, The glycinergic inhibitory synapse, Cell. Mol. Life Sci. 58 (2001) 760–793.
[85] H. Mizuno, M. Abe, P. Dedecker, A. Makino, S. Rocha, Y. Ohno-Iwashita, J. Hofkens, T. Kobayashi, A. Miyawaki, Fluorescent probes for superresolution imaging of lipid domains on the plasma membrane, Chem. Sci. 2 (2011) 1548–1553.
[86] K. Burger, G. Gimpl, F. Fahrenholz, Regulation of receptor function by cholesterol, Cell. Mol. Life Sci. 57 (2000) 1577–1592.
[87] R. Willmann, S. Pun, L. Stallmach, G. Sadasivam, A.F. Santos, P. Caroni, C. Fuhrer, Cholesterol and lipid microdomains stabilize the postsynapse at the neuromuscular junction, EMBO J. 25 (2006) 4050–4060.
[88] H.G. Breitinger, C. Villmann, N. Melzer, J. Rennert, U. Breitinger, S. Schwarzinger, C.M. Becker, Novel regulatory site within the TM3-4 loop of human recombinant alpha3 glycine receptors determines channel gating and domain structure, J. Biol. Chem. 284 (2009) 28624–28633.